Gradient-enhanced model and its micromorphic regularization for simulation of Lüders-like bands in shape memory alloys[☆]

Mohsen Rezaee Hajidehi[a], Stanisław Stupkiewicz[b,∗]

[a]*Department of Civil, Environmental, Aerospace Engineering and Materials (DICAM), University of Palermo,*
Viale delle Scienze Ed. 8, 90128 Palermo, Italy
[b]*Institute of Fundamental Technological Research (IPPT), Polish Academy of Sciences,*
Pawińskiego 5B, 02-106 Warsaw, Poland.

Abstract

Shape memory alloys, notably NiTi, often exhibit softening pseudoelastic response that results in formation and propagation of Lüders-like bands upon loading, for instance, in uniaxial tension. A common approach to modelling softening and strain localization is to resort to gradient-enhanced formulations that are capable of restoring well-posedness of the boundary-value problem. This approach is also followed in the present paper by introducing a gradient-enhancement into a simple one-dimensional model of pseudoelasticity. In order to facilitate computational treatment, a micromorphic-type regularization of the gradient-enhanced model is subsequently performed. The formulation employs the incremental energy minimization framework that is combined with the augmented Lagrangian treatment of the resulting non-smooth minimization problem. A thermomechanically coupled model is also formulated and implemented in a finite-element code. The effect of the loading rate on the localization pattern in a NiTi wire under tension is studied, and the features predicted by the model show a good agreement with the experimental observations. Additionally, an analytical solution is provided for a propagating interface (macroscopic transformation front) both for the gradient-enhanced model and for its micromorphic version.

Keywords: martensite, phase transformation, micromorphic model, strain localization, thermomechanical coupling

1. Introduction

Due to their unique thermomechanical properties, shape memory alloys (SMAs) have gained wide applicability in engineering and medicine and thus attract significant research interest (Otsuka and Wayman, 1999). The underlying effects, notably pseudoelasticity and shape memory effect, result from the martensitic phase transformation and are accompanied by formation and evolution of martensitic microstructures

---

at several scales (Bhattacharya, 2003). Numerous constitutive models have been developed to address various aspects of the complex behaviour of SMAs, from the atomistic to the macroscopic scale. A detailed overview of the constitutive models of SMAs available in the literature is beyond the scope of this paper, the reader is referred to recent reviews (e.g., Patoor et al., 2006; Lagoudas et al., 2006; Cisse et al., 2016).

It is commonly observed in the experiments that stress-induced pseudoelastic response of SMAs is accompanied by softening behaviour and strain localization. A typical example is the uniaxial tension of NiTi wires, strips and tubes (e.g., Shaw and Kyriakides, 1997; Sittner et al., 2005; Pieczyska et al., 2006; Favier et al., 2007; Daly et al., 2007; Zhang et al., 2010; Sedmák et al., 2016) in which transformation proceeds through nucleation and propagation of macroscopic transformation fronts so that the deformation pattern resembles Lüders bands. At low loading rates, i.e. in nearly isothermal conditions, the fronts propagate at an approximately constant load, thus a stress plateau is observed on the apparent stress–strain curve. A detailed study of the effect of the loading rate on the pattern of Lüders-like bands and on stress hysteresis in NiTi strips has been reported by Zhang et al. (2010). Localized deformation has been observed also in NiTi tubes under combined tension–torsion loading (Sun and Li, 2002) and under pure bending (Bechle and Kyriakides, 2014; Jiang et al., 2017a).

The typical mechanical response exhibiting a stress plateau is often incorrectly interpreted as the material response, while it is in fact the response of a specimen, which is related to nucleation and propagation of macroscopic transformation fronts. The actual material response involves softening, sometimes significant, which however cannot be directly observed due to localization phenomena. This has been very clearly illustrated by the careful experiment of Hallai and Kyriakides (2013), in which the intrinsic softening response of NiTi has been revealed by extracting it from the overall response of a uniformly deforming laminate composed of NiTi and steel sheets, the latter exhibiting a hardening elastoplastic response.

Implementation of the softening behaviour into a constitutive model usually does not constitute a difficulty. However, solution of the resulting boundary value problem is not immediate because the problem becomes ill-posed, which leads, for instance, to pathological mesh sensitivity. One way to regularize the problem is to enhance the model with non-local (Ahmadian et al., 2015) or gradient terms (Chang et al., 2006; Duval et al., 2011; Armattoe et al., 2014; Badnava et al., 2014; Alessi and Bernardini, 2015; León Baldelli et al., 2015). This introduces a characteristic length into the model so that diffuse transformation fronts are formed and a sharp transition from the transformed to non-transformed zone is penalized.

Note that a kind of regularization, which has a clear physical basis, is introduced by including the thermomechanical coupling and heat conduction. However, this regularization may be insufficient in nearly isothermal conditions, for instance, in the case of propagation of an existing macroscopic transformation front at a vanishingly small speed.

Interestingly, finite-element simulations of strain localization and Lüders-like bands in SMA strips and tubes under tension and tubes under bending have been successfully carried out by Jiang et al. (2017a,b,c)

using an isothermal, plasticity-like softening model with no regularization. A mild mesh dependence of the results has been observed, which can be explained by the three-dimensional through-thickness effects (Mazière and Forest, 2015).

In this work, a gradient-enhancement is introduced into a simple one-dimensional model of pseudoelasticity in SMAs. The starting point here is a one-dimensional small-strain version of the model of pseudoelasticity developed by Stupkiewicz and Petryk (2013), however, the approach is general and can be applied to virtually any macroscopic model, including extension to a three-dimensional model. The main focus of this work, and its original contribution, is a micromorphic regularization of the gradient-enhanced model and its energy-based incremental formulation. To this end, a new degree of freedom is introduced into the model that can be interpreted as a micromorphic counterpart of the volume fraction of martensite. The micromorphic approach adopted here is similar to that of Mazière and Forest (2015) that has been developed for modelling of softening–hardening plasticity leading to formation of Lüders bands in metals. The resulting micromorphic model is suitable for a direct finite-element implementation based on the incremental energy minimization approach combined with the augmented Lagrangian treatment of the resulting non-smooth minimization problem. An analytical solution is also provided for a propagating phase transformation interface (macroscopic transformation front) both for the gradient-enhanced model and for the micromorphic one. Finally, a thermomechanically coupled model is formulated and implemented in a finite-element code. Using this model, uniaxial tension of a NiTi wire is simulated, and the effect of loading rate on the localization pattern is studied. The results obtained show a good agreement with the experiment.

2. One-dimensional model of pseudoelasticity

In order to concentrate on the most essential feature, i.e. on gradient enhancement and its micromorphic regularization, the model discussed in this paper is restricted to one-dimensional pseudoelastic response in tension at small strain. A sequence of isothermal models is discussed first, starting from a local model, through its gradient-enhanced version, to finally arrive at a micromorphic model. Subsequently, the most essential thermomechanical coupling terms are accounted for, thus leading to a coupled thermomechanical model. The isothermal local model discussed below is essentially a one-dimensional version of the general three-dimensional model of Stupkiewicz and Petryk (2013).

Despite the model is one-dimensional, in the notation we will use ∇ and $\nabla \cdot$ to denote the gradient and divergence, respectively, so that the structure of the model resembles that of the corresponding three-dimensional model to be developed in the future. Clearly, in one-dimension, the two operations reduce to the usual spatial derivative.

2.1. Local model

The total strain $\varepsilon = e(u)$, where $e(u) = \nabla u$ and u denotes the displacement, is decomposed into its elastic ε_e and inelastic (transformation) ε_t parts,

$$\varepsilon = \varepsilon_e + \varepsilon_t, \qquad \varepsilon_t = \eta \bar{\epsilon}_t, \qquad 0 \leq \eta \leq 1, \tag{1}$$

where η denotes the volume fraction of martensite, and $\bar{\epsilon}_t$ is a model parameter. Here, we rely on the assumption that, in the pseudoelastic regime, martensite is fully oriented, and $\bar{\epsilon}_t$ is its transformation strain. Since only tension is considered, we have $\bar{\epsilon}_t > 0$.

The function specifying the Helmholtz free energy (per unit volume) in isothermal conditions is adopted in the following form (cf. Stupkiewicz and Petryk, 2013),

$$\phi(\varepsilon, \eta) = \phi_0 + \Delta\phi_0 \eta + \frac{1}{2} E (\varepsilon - \eta \bar{\epsilon}_t)^2 + \frac{1}{2} H \eta^2, \tag{2}$$

where ϕ_0 is the free energy of austenite in a stress-free state, $\Delta\phi_0$ is the chemical energy, E is the Young's modulus, and H is the parameter controlling the hardening or softening associated with increasing η. We assume here that H is non-negative, $H \geq 0$, because for $H < 0$ a softening response is obtained, as shown later, and the problem is then ill-posed. A negative hardening parameter will be admitted in the gradient-enhanced model discussed in Section 2.2.

The Helmholtz free energy functional $\Phi[u, \eta]$ is obtained by integrating ϕ over the body domain B,

$$\Phi[u, \eta] = \int_B \phi(e(u), \eta) \, \mathrm{d}V, \tag{3}$$

and the potential energy is defined as

$$\mathcal{E}[u, \eta] = \Phi[u, \eta] + \Omega[u], \tag{4}$$

where $\Omega[u]$ is the potential energy of external loads, which are assumed conservative.

In the incremental (finite-step) formulation, the rate-independent dissipation is governed by the following dissipation potential,

$$\Delta D(\Delta \eta) = f_c |\Delta \eta|, \qquad f_c > 0, \qquad \Delta \eta = \eta - \eta_n, \tag{5}$$

and its global counterpart,

$$\Delta \mathcal{D}[\eta] = \int_B \Delta D(\eta - \eta_n) \, \mathrm{d}V, \tag{6}$$

where f_c is the critical driving force, and η_n is the martensite volume fraction at the end of the previous step. Note that quantities without a subscript refer to the current time instant $t = t_{n+1}$.

The incremental solution, i.e. the *fields* of displacement u and volume fraction η at the current instant t_{n+1}, are determined by minimization of the *global* incremental potential $\Pi[u, \eta]$ (cf., Petryk, 2003; Stupkiewicz and Petryk, 2013),

$$\{u, \eta\} = \arg \min_{u, \eta} \, \Pi[u, \eta], \tag{7}$$

4

where

$$\Pi[u, \eta] = \mathcal{E}[u, \eta] - \mathcal{E}[u_n, \eta_n] + \Delta\mathcal{D}[\eta] + \mathcal{I}[\eta], \tag{8}$$

and u is here implicitly assumed to satisfy the Dirichlet boundary condition. The last term in Eq. (8) enforces the physical constraint $0 \leq \eta \leq 1$ by employing the indicator function $I_{[0,1]}(\eta)$,

$$\mathcal{I}[\eta] = \int_B I_{[0,1]}(\eta)\mathrm{d}V, \qquad I_{[0,1]}(\eta) = \begin{cases} 0 & \text{if } 0 \leq \eta \leq 1, \\ +\infty & \text{otherwise.} \end{cases} \tag{9}$$

Because of the last two terms in the incremental potential (8), the minimization problem (7) is non-smooth.

Following the standard argument, minimization of $\Pi[u, \eta]$ with respect to the displacement field u, for a fixed field of η, yields a stable equilibrium of the body, and the necessary condition for the minimum gives the equilibrium equation in a weak form. In the absence of body forces, the standard local equilibrium equation is then obtained,

$$\nabla \cdot \sigma = 0, \qquad \sigma = E(\varepsilon - \eta\bar{\epsilon}_t), \tag{10}$$

where σ is the stress. In one-dimensional setting, the equilibrium equation trivially implies that the stress is constant.

Since the free energy $\phi(\varepsilon, \eta)$ depends on η and does not depend on its gradient, minimization of $\Pi[u, \eta]$ with respect to the field of η, for a fixed displacement field u, can be performed locally at each point. The corresponding *local* minimization problem amounts to minimizing the incremental energy density $\pi(\varepsilon, \eta)$ at fixed ε,

$$\eta = \arg\min_\eta \pi(\varepsilon, \eta), \qquad \pi(\varepsilon, \eta) = \phi(\varepsilon, \eta) - \phi(\varepsilon_n, \eta_n) + \Delta D(\eta - \eta_n) + I_{[0,1]}(\eta). \tag{11}$$

It can be checked that the free energy function $\phi(\varepsilon, \eta)$ is convex in η when $H \geq -E\bar{\epsilon}_t^2$. The remaining two terms of $\pi(\varepsilon, \eta)$ are also convex, though non-smooth. Accordingly, the minimum exists and satisfies the inclusion $0 \in \partial\pi_\varepsilon(\eta)$, where $\pi_\varepsilon(\eta) = \pi(\varepsilon, \eta)$ for given ε, which can be rewritten in the following form,

$$f \in \partial\bar{D}(\eta), \qquad \bar{D}(\eta) = \Delta D(\eta - \eta_n) + I_{[0,1]}(\eta), \tag{12}$$

where f is the thermodynamic driving force,

$$f = -\frac{\partial\phi}{\partial\eta} = -\Delta\phi_0 + \sigma\bar{\epsilon}_t - H\eta, \tag{13}$$

and $\bar{D}(\eta)$ groups the non-smooth part of $\pi(\varepsilon, \eta)$. Here, $\partial(\cdot)$ denotes the subdifferential which is a generalization of the derivative to non-smooth functions (Rockafellar, 1970), see also (Moreau, 1974). Figure 1 shows the graphs of the non-smooth function $\bar{D}(\eta)$ and its subdifferential $\partial\bar{D}(\eta)$, see also (Stupkiewicz and Petryk, 2013; Tůma et al., 2017).

When the transformation proceeds with non-zero $\Delta\eta$, and the bound constraints are not active, i.e. $0 < \eta < 1$, inclusion (12) yields the following transformation criterion,

$$f = \pm f_c \quad \Leftrightarrow \quad \sigma_t^\pm = \frac{\Delta\phi_0 \pm f_c + H\eta}{\bar{\epsilon}_t}, \tag{14}$$
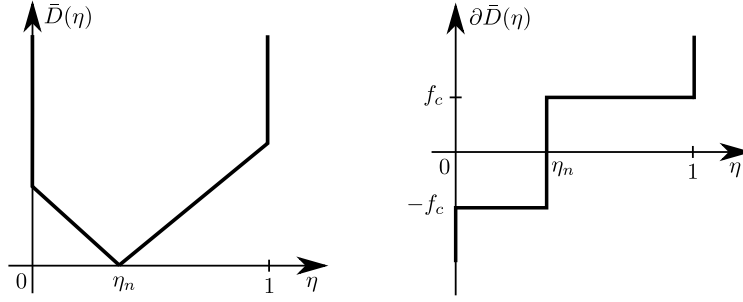
5

Figure 1: Graphs of the non-smooth part $\bar{D}(\eta)$, Eq. (12), of the incremental potential $\pi(\varepsilon, \eta)$ (left) and its subdifferential (right).
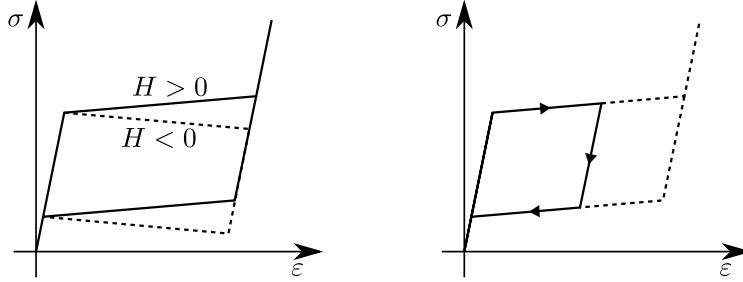

Figure 2: The stress-strain response resulting from the model in the case of complete (left) and incomplete (right) transformation.

where σ_t^+ (σ_t^-) is the transformation stress during forward (reverse) transformation with $\Delta \eta > 0$ ($\Delta \eta < 0$). It follows that $H > 0$ and $H < 0$ indeed imply, respectively, a hardening and softening response. The stress-strain response resulting from the present one-dimensional model is illustrated in Fig. 2.

2.2. Gradient-enhanced model

A possible approach to circumvent the ill-conditioning resulting from the softening response for $H < 0$ is to enhance the model with a gradient term. In the present context of pseudoelasticity in SMAs, it is natural to formulate the gradient contribution in terms of η, the volume fraction of martensite. The free energy function is thus assumed in the following form,

$$\phi_g(\varepsilon, \eta, \nabla\eta) = \phi(\varepsilon, \eta) + \frac{1}{2}G\left|\nabla\eta\right|^2, \tag{15}$$

where G is a positive parameter. The gradient enhancements of the type adopted above, or introduced directly into the transformation (or yield, damage, etc.) criterion, are known to deliver regularization for models exhibiting softening and strain localization in damage and softening plasticity (e.g., Aifantis, 1984; Peerlings et al., 1996; de Borst et al., 1999; Geers, 2004), in softening–hardening plasticity leading to Lüders bands (e.g., Mühlhaus and Boland, 1991; Mazière and Forest, 2015), and in softening pseudoelasticity (e.g., Duval et al., 2011; Alessi and Bernardini, 2015; León Baldelli et al., 2015).

6

The Helmholtz free energy functional $\Phi_g[u, \eta]$ of the gradient-enhanced model and the corresponding potential energy $\mathcal{E}_g[u, \eta]$ are defined as

$$\Phi_g[u, \eta] = \int_B \phi_g(e(u), \eta, \nabla\eta) \, dV, \qquad \mathcal{E}_g[u, \eta] = \Phi_g[u, \eta] + \Omega[u]. \tag{16}$$

The *global* incremental potential $\Pi_g[u, \eta]$, which takes the following form

$$\Pi_g[u, \eta] = \mathcal{E}_g[u, \eta] - \mathcal{E}_g[u_n, \eta_n] + \Delta\mathcal{D}[\eta] + \mathcal{I}[\eta], \tag{17}$$

is then minimized to yield the incremental solution in terms of the *fields* of u and η at instant t_{n+1},

$$\{u, \eta\} = \arg\min_{u, \eta} \Pi_g[u, \eta]. \tag{18}$$

As before, the minimization with respect to the displacement field u for fixed η, in the absence of body force, yields the standard equilibrium equation (10).

The free energy $\phi_g(\varepsilon, \eta, \nabla\eta)$ depends now on the value of η and its gradient $\nabla\eta$. Therefore, the minimization of $\Pi_g[u, \eta]$ with respect to the field of η can not be performed locally as in the case of the local model, cf. Eqs. (11) and (12). However, a similar structure of the necessary condition for the minimum of $\Pi_g[u, \eta]$ with respect to η is obtained,

$$f_g \in \partial\bar{D}(\eta), \tag{19}$$

by introducing the thermodynamic driving force f_g,

$$f_g = -\frac{\delta\Phi_g}{\delta\eta} = f + G\nabla^2\eta, \tag{20}$$

where

$$\frac{\delta\Phi_g}{\delta\eta} = \frac{\partial\Phi_g}{\partial\eta} - \nabla \cdot \frac{\partial\Phi_g}{\partial\nabla\eta}, \tag{21}$$

is the classical functional derivative of Φ_g, f is the driving force in the local model and is given by Eq. (13) and ∇^2 denotes the Laplacian operator, i.e. the second spatial derivative in one-dimensional case. The differential inclusion (19) is accompanied by the homogeneous Neumann boundary condition, $\nabla_n\eta = 0$, on the boundary of the body domain B.

Assuming that the transformation proceeds with $\Delta\eta \neq 0$ and $0 < \eta < 1$, the transformation stress in the gradient-enhanced model is obtained from the inclusion (19) in the following form,

$$f_g = \pm f_c \quad \Leftrightarrow \quad \sigma_{t,g}^{\pm} = \frac{\Delta\phi_0 \pm f_c + H\eta - G\nabla^2\eta}{\bar{\epsilon}_t}. \tag{22}$$

It follows that, compared to the local model, cf. Eq. (14), the transformation stress depends on the Laplacian of η. Equation (22) is the starting point for deriving an analytical solution for a propagating interface, see Section 3.1.

7

2.3. Micromorphic model

Direct implementation of the gradient-enhanced model of the previous section is not straightforward because the transformation criterion (19), which governs the evolution of η, involves the Laplacian of η. To facilitate the finite-element implementation, a micromorphic regularization of the gradient-enhanced model is here performed by introducing an additional variable $\bar{\eta}$, as a micromorphic counterpart of η. The present approach is similar to that used by Mazière and Forest (2015) to model softening–hardening plasticity, see also Forest (2016) for a general overview of the micromorphic regularization approach. However, the present formulation relies on incremental energy minimization, and we do not explicitly resort to generalized stresses. In fact, the corresponding balance equation is obtained directly as the necessary condition for the minimum of an incremental potential.

The free energy function is thus adopted in the following form,

$$\phi_\mu(\varepsilon, \eta, \bar{\eta}, \nabla\bar{\eta}) = \phi(\varepsilon, \eta) + \frac{1}{2}\chi(\eta - \bar{\eta})^2 + \frac{1}{2}G\left|\nabla\bar{\eta}\right|^2, \tag{23}$$

where, compared to $\phi_g(\varepsilon, \eta, \nabla\eta)$ in Eq. (15), the gradient term is expressed in terms of the new variable $\bar{\eta}$, and an additional term is introduced, which penalizes deviation of $\bar{\eta}$ from η, with $\chi > 0$ being the corresponding model parameter (it is discussed later that χ must satisfy a stronger condition, $\chi > -H > 0$, when $H < 0$).

The free energy functional $\Phi_\mu[\varepsilon, \eta, \bar{\eta}]$ and the corresponding potential energy $\mathcal{E}_\mu[u, \eta, \bar{\eta}]$ are now defined as,

$$\Phi_\mu[u, \eta, \bar{\eta}] = \int_B \phi_\mu(e(u), \eta, \bar{\eta}, \nabla\bar{\eta})\,\mathrm{d}V, \qquad \mathcal{E}_\mu[u, \eta, \bar{\eta}] = \Phi_\mu[u, \eta, \bar{\eta}] + \Omega[u]. \tag{24}$$

Since a new degree of freedom is added to the problem, the minimization of the *global* incremental potential

$$\Pi_\mu[u, \eta, \bar{\eta}] = \mathcal{E}_\mu[u, \eta, \bar{\eta}] - \mathcal{E}_\mu[u_n, \eta_n, \bar{\eta}_n] + \Delta\mathcal{D}[\eta] + \mathcal{I}[\eta], \tag{25}$$

is now performed with respect to *fields* of u, η and $\bar{\eta}$,

$$\{u, \eta, \bar{\eta}\} = \arg\min_{u,\eta,\bar{\eta}}\,\Pi_\mu[u, \eta, \bar{\eta}]. \tag{26}$$

Again, for fixed η and $\bar{\eta}$, the local equilibrium equation in Eq. (10) is found by minimizing $\Pi_\mu[u, \eta, \bar{\eta}]$ with respect to the displacement field u.

As in the case of the local model, the free energy $\phi_\mu(\varepsilon, \eta, \bar{\eta}, \nabla\bar{\eta})$ is merely dependent on η and not its gradient. As a result, the minimization of $\Pi_\mu[u, \eta, \bar{\eta}]$ with respect to η can be carried out locally. This is, in fact, the main reason for introducing the micromorphic regularization of the gradient-enhanced model. For fixed ε, $\bar{\eta}$ and $\nabla\bar{\eta}$, the *local* minimization problem reads

$$\eta = \arg\min_\eta \pi_\mu(\varepsilon, \eta, \bar{\eta}, \nabla\bar{\eta}), \tag{27}$$

where

$$\pi_\mu(\varepsilon, \eta, \bar{\eta}, \nabla\bar{\eta}) = \phi_\mu(\varepsilon, \eta, \bar{\eta}, \nabla\bar{\eta}) - \phi_\mu(\varepsilon_n, \eta_n, \bar{\eta}_n, \nabla\bar{\eta}_n) + \Delta D(\eta - \eta_n) + I_{[0,1]}(\eta). \tag{28}$$

Convexity of $\phi_\mu(\varepsilon, \eta, \bar{\eta})$ and $\pi_\mu(\varepsilon, \eta, \bar{\eta}, \nabla\bar{\eta})$ in η is ensured if $H \geq -E\bar{\epsilon}_t^2 - \chi$. The necessary condition for the minimum (27) is now

$$f_\mu \in \partial\bar{D}(\eta), \tag{29}$$

and is expressed in terms of the thermodynamic driving force f_μ,

$$f_\mu = -\frac{\partial\phi_\mu}{\partial\eta} = f - \chi(\eta - \bar{\eta}), \tag{30}$$

where f is given by Eq. (13). For $\Delta\eta \neq 0$ and $0 < \eta < 1$, inclusion (30) gives the following expression for the transformation stress,

$$f_\mu = \pm f_c \quad \Leftrightarrow \quad \sigma_{t,\mu}^\pm = \frac{\Delta\phi_0 \pm f_c + H\eta + \chi(\eta - \bar{\eta})}{\bar{\varepsilon}_t}. \tag{31}$$

Finally, minimization of $\Pi_\mu[\varepsilon, \eta, \bar{\eta}, \nabla\bar{\eta}]$ with respect to the field of $\bar{\eta}$ yields the following necessary condition:

$$\frac{\delta\Pi_\mu}{\delta\bar{\eta}} = 0, \tag{32}$$

where $\frac{\delta\Pi_\mu}{\delta\bar{\eta}}$ is the functional derivative of Π_μ, cf. Eq. (21). Since Π_μ depends on $\bar{\eta}$ only through Φ_μ, we have

$$\frac{\delta\Pi_\mu}{\delta\bar{\eta}} = \frac{\delta\Phi_\mu}{\delta\bar{\eta}} = -\chi(\eta - \bar{\eta}) - G\nabla^2\bar{\eta} = 0. \tag{33}$$

The micromorphic variable $\bar{\eta}$ is thus governed by the following differential equation,

$$\bar{\eta} - \ell^2\nabla^2\bar{\eta} = \eta, \qquad \ell = \sqrt{\frac{G}{\chi}}, \tag{34}$$

where ℓ is the internal length related to the averaging operation delivered by Eq. (34). The Helmholtz-type equation (34) is the same as the one frequently used for regularization of damage or softening plasticity within the so-called implicit-gradient approach (Peerlings et al., 1996; Geers, 2004), see also (Mazière and Forest, 2015).

Equation (34) is accompanied here by the homogeneous Neumann boundary condition, $\nabla_n\bar{\eta} = 0$, on the boundary of the body domain B. The above Neumann type-boundary condition together with Eq. (34) implies that $\int_B \eta\,\mathrm{d}V = \int_\mathrm{B} \bar{\eta}\,\mathrm{d}V$. This property would not hold for a Dirichlet boundary condition, which might be used, for instance, to define a non-transforming boundary.

From Eq. (33) it follows that $\chi(\eta - \bar{\eta}) = -G\nabla^2\bar{\eta}$, so that the term $\chi(\eta - \bar{\eta})$ in the expression (31) for the transformation stress $\sigma_{t,\mu}^\pm$ can be replaced by $-G\nabla^2\bar{\eta}$. Now, when χ is sufficiently high, $\bar{\eta}$ is close to η, and thus $\nabla^2\bar{\eta}$ is close to $\nabla^2\eta$. It follows that, in the limit, the micromorphic model is equivalent to the gradient-enhanced model, and in particular we have $f_\mu \approx f_g$, and $\sigma_{t,\mu}^\pm \approx \sigma_{t,g}^\pm$.

2.4. *Thermomechanically coupled model*

A simple extension of the above micromorphic model to the thermomechanically coupled case is here developed by considering heat conduction and two most essential thermomechanical couplings. Firstly, the

dependence of the chemical energy $\Delta\phi_0$ on the temperature is accounted for, thus introducing dependence of the mechanical response on the temperature. Secondly, the latent heat of transformation, which is associated with the exothermic and endothermic nature of, respectively, forward and reverse transformations, and the dissipated energy are introduced into the heat equation as a source term, so that inhomogeneous deformation results in temperature inhomogeneity and in heat conduction. Note that other couplings, including thermal expansion and temperature-dependence of material constants, which are secondary effects, are neglected in the present simple model.

The free energy density of a pure austenite phase in a stress-free condition, ϕ_0^a, and that of a pure martensite phase, ϕ_0^m, are defined as (Raniecki et al., 1992),

$$\phi_0^a = \phi_0(T) + u_0^a - Ts_0^a, \qquad \phi_0^m = \phi_0(T) + u_0^m - Ts_0^m, \tag{35}$$

where u_0^a and u_0^m are the internal energy densities of, respectively, austenite and martensite phases in the reference state (i.e. in the stress-free condition at $T = T_0$), s_0^a and s_0^m are the entropies of, respectively, austenite and martensite phases in the reference state, and $\phi_0(T) = \rho c(T - T_0 - T\log(T/T_0))$, where T and T_0 are the current and reference temperatures, respectively, and ρc is the specific heat per unit volume.

The chemical energy, $\Delta\phi_0$, that appears in Eq. (2) is then obtained as a linear function of temperature,

$$\Delta\phi_0(T) = \phi_0^m - \phi_0^a = -\Delta u^* + \Delta s^* T = \Delta s^*(T - T_t), \tag{36}$$

where $\Delta u^* = u_0^a - u_0^m > 0$, $\Delta s^* = s_0^a - s_0^m > 0$, and $T_t = \frac{\Delta u^*}{\Delta s^*}$ is the transformation (equilibrium) temperature. It follows that the chemical energy $\Delta\phi_0$ increases with increasing temperature, for instance, during forward transformation ($\dot\eta > 0$), which is exothermic. In non-isothermal conditions, the transformation stress will thus increase (decrease) during forward (reverse) transformation due to the latent heat of transformation, cf. Eqs. (14), (22) and (31).

The local heat source results from the latent heat of transformation and from mechanical dissipation. Specifically, the volumetric heat source $\dot q_v$ is expressed as,

$$\dot q_v = \Delta s^* T\dot\eta + f_c|\dot\eta|, \tag{37}$$

where a superposed dot denotes the time derivative. The first term, which corresponds to the latent heat of transformation, controls the exothermic and endothermic reactions of the forward (with $\dot\eta > 0$) and reverse (with $\dot\eta < 0$) transformations, respectively. Finally, the local heat equation takes the form,

$$\rho c\dot T = \dot q_v + \kappa\nabla^2 T, \tag{38}$$

where κ is the thermal conductivity.

3. Analytical solution for a propagating phase transformation interface

In this section, an analytical solution is derived for a phase transformation interface propagating in isothermal conditions for the gradient-enhanced model and for the micromorphic one. It is shown that
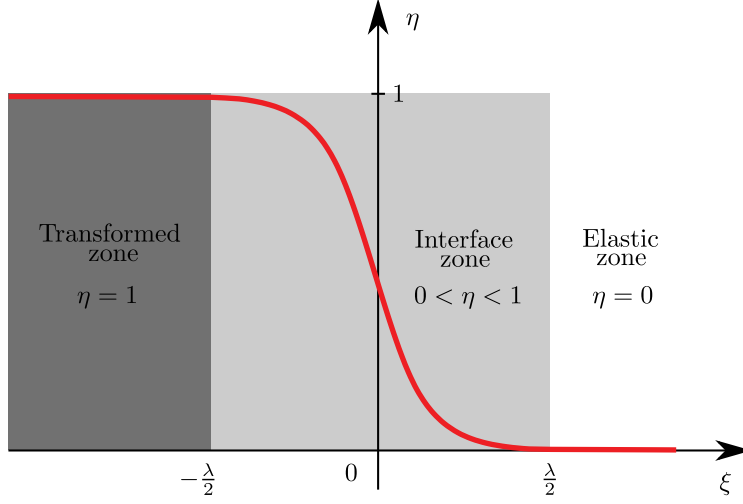
Figure 3: Illustration of the phase transformation interface in the gradient-enhanced model.

the solution of the gradient-enhanced model is equivalent to the micromorphic one in the limit when the local volume fraction of martensite η coincides with its micromorphic counterpart $\bar{\eta}$. In numerical implementation, this can be achieved by taking χ as large as possible to reduce the difference between the two quantities (as discussed in Section 3.2). The analytical solutions are obtained for a material with a softening response, i.e. for $H < 0$, when transformation localizes and an interface can be formed, and assuming forward transformation, i.e. $\Delta \eta > 0$.

3.1. Analytical solution for the gradient-enhanced model

Consider the phase transformation interface in Fig. 3 that is generated in an SMA rod. The local coordinate system is set such that $\xi = 0$ corresponds to the position of the interface (precisely, to its centre where $\eta = \frac{1}{2}$). Three zones are introduced. In the elastic (non-transformed) zone, for $\xi \geq \frac{1}{2}\lambda$, we have $\eta = 0$, and in the fully transformed zone, for $\xi \leq -\frac{1}{2}\lambda$, we have $\eta = 1$. The diffuse interface with $0 < \eta < 1$ occupies the zone $-\frac{1}{2}\lambda < \xi < \frac{1}{2}\lambda$, and λ denotes the thickness of the diffuse interface, to be determined below.

The formula (22) for the transformation stress during forward transformation can be rewritten in the following form,

$$\eta'' + \omega^2 \eta = \omega^2 R, \tag{39}$$

where η'' denotes the second derivative of η with respect to ξ and

$$\omega = \sqrt{\frac{-H}{G}}, \qquad R = \frac{\sigma_{t,g}^+ \bar{\epsilon}_t - \Delta\phi_0 - f_c}{H}. \tag{40}$$

The solution of the differential equation (39) is obtained as,

$$\eta(\xi) = \alpha_1 \sin(\omega\xi) + \alpha_2 \cos(\omega\xi) + R. \tag{41}$$

11

where α_1 and α_2 are the integration constants to be determined by using boundary conditions. The boundary conditions are specified by enforcing the continuity of η and its derivative at the boundary between the elastic and the interface zone as well as between the transformed and the interface zone, viz.

$$\eta(-\tfrac{1}{2}\lambda) = 1, \qquad \eta'(-\tfrac{1}{2}\lambda) = 0, \qquad \eta(\tfrac{1}{2}\lambda) = 0, \qquad \eta'(\tfrac{1}{2}\lambda) = 0. \tag{42}$$

Note that $\sigma_{t,g}^+$ and λ constitute here additional unknowns to be determined such that all boundary conditions are satisfied. As a result, the following solution is obtained for the volume fraction η,

$$\eta(\xi) = \begin{cases} 1 & \xi \leq -\tfrac{1}{2}\lambda, \\ \tfrac{1}{2}(1 - \sin(\omega\xi)) & -\tfrac{1}{2}\lambda < \xi < \tfrac{1}{2}\lambda, \\ 0 & \xi \geq \tfrac{1}{2}\lambda, \end{cases} \tag{43}$$

and for the interface thickness λ,

$$\lambda = \frac{\pi}{\omega}. \tag{44}$$

It also follows that $R = \tfrac{1}{2}$, which after substitution in Eq. $(40)_2$ gives the value of the transformation stress, which corresponds to the Maxwell stress,

$$\sigma_{t,g}^+ = \frac{\Delta\phi_0 + f_c + \tfrac{1}{2}H}{\bar{\epsilon}_t}. \tag{45}$$

It can be checked that the above solution exactly corresponds to the diffuse interface in the phase-field model employing the so-called 'double-obstacle' potential (cf. Steinbach, 2009).

3.2. Analytical solution for the micromorphic model

The analytical solution corresponding to the micromorphic model is sketched in Fig. 4. As previously, the elastic and transformed zones correspond to $\eta = 0$ and $\eta = 1$, respectively, and η takes intermediate values in the interface zone. The non-local variable $\bar{\eta}$, which is obtained by averaging the local variable η according to Eq. (34), attains the limit values of 0 and 1 asymptotically. It is convenient to exploit the symmetry with respect to $\xi = 0$ and to derive the solution for one half of the domain, $\xi \geq 0$.

The following algebraic relation between η and $\bar{\eta}$ in the interface zone results from formula (31) for the transformation stress $\sigma_{t,\mu}^+$,

$$\eta = \frac{H\bar{R} + \chi\bar{\eta}}{\chi + H} \qquad \text{for} \quad \chi > -H > 0, \tag{46}$$

where

$$\bar{R} = \frac{\sigma_{t,\mu}^+ \bar{\epsilon}_t - \Delta\phi_0 - f_c}{H}. \tag{47}$$

Equations (34) and (46) furnish the following differential equation for $\bar{\eta}$ in the interface zone,

$$\bar{\eta}'' + \bar{\omega}^2\bar{\eta} = \bar{\omega}^2\bar{R}, \tag{48}$$
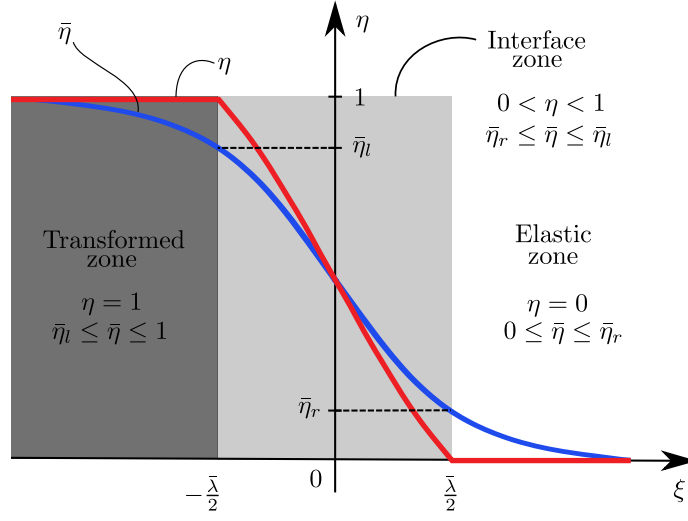
Figure 4: Illustration of the phase transformation interface in the micromorphic model: the local volume fraction η is denoted by the red line and the micromorphic variable $\bar{\eta}$ by the blue line.

where

$$\bar{\omega} = \sqrt{\frac{-H}{\ell^2(\chi + H)}} = \omega\sqrt{\frac{1}{1 - \ell^2\omega^2}}, \tag{49}$$

with the following solution,

$$\bar{\eta}(\xi) = \beta_1 \sin(\bar{\omega}\xi) + \beta_2 \cos(\bar{\omega}\xi) + \bar{R} \qquad \text{for} \quad 0 \leq \xi \leq \tfrac{1}{2}\bar{\lambda}. \tag{50}$$

The differential equation for $\bar{\eta}$ in the elastic zone is obtained from Eq. (34) by imposing $\eta = 0$, thus

$$\bar{\eta} - \ell^2\bar{\eta}'' = 0, \tag{51}$$

which yields the following solution,

$$\bar{\eta}(\xi) = \gamma_1 e^{\xi/\ell} + \gamma_2 e^{-\xi/\ell} \qquad \text{for} \quad \xi \geq \tfrac{1}{2}\bar{\lambda}. \tag{52}$$

Equations (48) and (51) involve four integration constants (β_1, β_2, γ_1, γ_2) to be determined by using boundary conditions. Here, like in the gradient-enhanced model, $\sigma_{t,\mu}^+$ and $\bar{\lambda}$ are two additional unknowns. The boundary conditions are specified by enforcing the continuity of $\bar{\eta}$ and its derivative between the interface and the elastic zone, the continuity of η between the interface and the elastic zone and the symmetry of the solution, i.e.,

$$\bar{\eta}_-(\tfrac{1}{2}\lambda) = \bar{\eta}_+(\tfrac{1}{2}\lambda), \quad \bar{\eta}'_-(\tfrac{1}{2}\lambda) = \bar{\eta}'_+(\tfrac{1}{2}\lambda), \quad \eta(\tfrac{1}{2}\bar{\lambda}) = 0, \quad \bar{\eta}(\infty) = 0, \quad \eta(0) = \bar{\eta}(0) = \tfrac{1}{2}. \tag{53}$$

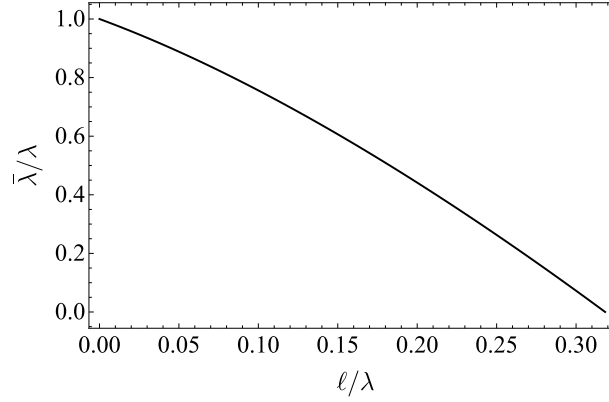The six unknown parameters can now be determined using the six boundary conditions (53). As a result, the

13

Figure 5: Dependence of the thickness $\bar{\lambda}$ of the phase transformation interface in the micromorphic model on the internal length ℓ, both normalized by λ, cf. Eq. (57).

following solution for $\bar{\eta}$ is obtained,

$$
\bar{\eta}(\xi) = \begin{cases} 1 + \dfrac{H}{2G}\, \mathrm{e}^{\xi/\ell} & \xi \le -\tfrac{1}{2}\bar{\lambda}, \\[2ex] \dfrac{1}{2} - \dfrac{(H+\chi)}{2G}\, \dfrac{\sin(\bar{\omega}\xi)}{\sin(\tfrac{1}{2}\bar{\omega}\bar{\lambda})} & -\tfrac{1}{2}\bar{\lambda} < \xi < \tfrac{1}{2}\bar{\lambda}, \\[2ex] -\dfrac{H}{2G}\, \mathrm{e}^{-\xi/\ell} & \xi \ge \tfrac{1}{2}\bar{\lambda}, \end{cases}
\tag{54}
$$

and the interface thickness $\bar{\lambda}$ is given by

$$
\bar{\lambda} = \frac{2}{\bar{\omega}} \arctan\left(\frac{-(H+\chi)\bar{\omega}\ell}{H} \right).
\tag{55}
$$

As previously, the Maxwell stress results from the condition $\bar{R} = \tfrac{1}{2}$,

$$
\sigma_{t,\mu}^{+} = \frac{\Delta\phi_0 + f_c + \tfrac{1}{2}H}{\bar{\epsilon}_t}.
\tag{56}
$$

It is interesting to examine the relationship between the interface thicknesses of the gradient-enhanced and micromorphic solutions. The following formula results from Eq. (55),

$$
\frac{\bar{\lambda}}{\lambda} = \frac{2}{\pi} \sqrt{1 - \left(\frac{\pi\ell}{\lambda}\right)^2} \arctan\left(\sqrt{\left(\frac{\lambda}{\pi\ell}\right)^2 - 1} \right),
\tag{57}
$$

and is depicted in Fig. 5. It follows that the solution of the micromorphic model converges to that of the gradient-enhanced one, i.e. $\bar{\lambda} \to \lambda$, when parameter χ is sufficiently large so that $\ell/\lambda \to 0$. On the other hand, when $\ell/\lambda \to 1/\pi$, the interface thickness $\bar{\lambda}$ approaches zero. This limit case corresponds to $\chi = -H$, cf. Eq. (46).

Figure 6 shows the profiles of η and $\bar{\eta}$ corresponding to $\ell/\lambda = 0.2$ and $\ell/\lambda = 0.05$. In the latter case, the two curves can be hardly distinguished, and they approximately coincide with the solution of the gradient-enhanced model (dashed lines in Fig. 6). The markers in Fig. 6 denote the finite-element solutions obtained
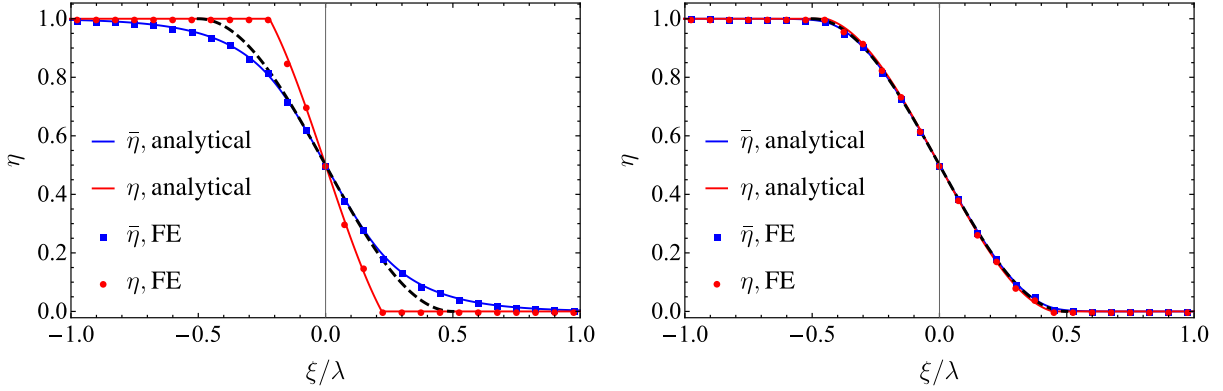
14

Figure 6: Phase transformation interface in the micromorphic model: profiles of η and $\bar{\eta}$ for $\frac{\ell}{\lambda} = 0.2$ (left) and $\frac{\ell}{\lambda} = 0.05$ (right). The dashed lines correspond to the analytical solution for the gradient-enhanced model.

using a relatively fine mesh with $h/\lambda = 0.075$, where h is the mesh size (the finite-element formulation is discussed in Section 4.1).

4. Uniaxial tension of a NiTi wire

4.1. Finite element implementation

The coupled thermomechanical problem at hand is governed by the minimization problem (26) (the mechanical part) and by the heat equation (38) (the thermal part). Finite element treatment of both subproblems is briefly described below. Standard details are omitted for brevity.

As discussed in Section 2.3, the incremental potential (25) is non-smooth in the local variable η, however, the corresponding minimization can be performed locally, e.g., at each Gauss point in the finite element implementation. Here, following Stupkiewicz and Petryk (2013), the augmented Lagrangian method is used to transform the non-smooth constrained minimization in terms of η to a smooth unconstrained saddle-point problem in terms of η and a single Lagrange multiplier that treats both the non-smooth dissipation function and the bound constraints on η. One can show that, at the solution, the Lagrange multiplier is equal to the driving force f_μ and thus satisfies inclusion (29). For details the reader is referred to Stupkiewicz and Petryk (2013) and Tůma et al. (2017).

The remaining minimization with respect to the fields of displacement u and non-local volume fraction $\bar{\eta}$ is performed by solving the equations that express the necessary condition for the minimum, i.e., stationarity of the incremental functional Π_μ with respect to the fields of u and $\bar{\eta}$. The resulting weak forms constitute the basis for the finite-element implementation of the mechanical subproblem with global unknowns u and $\bar{\eta}$.

With regard to the thermal subproblem, the local heat equation (38) is transformed into its global weak form in a standard way, and the implicit backward-Euler scheme is used for time discretization.

15

The complete problem involves thus three global fields $(u, \bar{\eta}, T)$. In the finite-element discretization, the displacement field u is approximated using piecewise-quadratic basis functions, while $\bar{\eta}$ and T are approximated using piecewise-linear basis functions. The resulting discrete finite-element equations are solved in a monolithic manner using the Newton method. The exact algorithmic tangent is derived by considering the thermomechanical couplings discussed in Section 2.4. Computer implementation has been performed using the *AceGen/AceFEM* system (Korelc, 2009; Korelc and Wriggers, 2016). In particular, the automatic differentiation (AD) technique implemented in *AceGen* has been used to automatically derive the exact algorithmic tangent. The analytical solution derived is Section 3 has been used to verify the correctness of the finite-element formulation and implementation, see Fig. 6.

4.2. Problem description

The uniaxial response of a NiTi wire under tension is studied as an application of the model developed above. The main focus of this numerical example is to show the suitability of the proposed micromorphic formulation to describe nucleation and propagation of macroscopic transformation fronts. Having this modelling tool, the effect of the loading rate on the force-displacement response, transformation pattern and temperature field is also studied. Material parameters have been adopted such that the model predictions are qualitatively comparable to the experimental results of Zhang et al. (2010). However, it is not our aim to reproduce those results exactly, as the present model is one-dimensional, which is a significant simplification with respect to the experimental setup of Zhang et al. (2010).

The one-dimensional wire model is sketched in Fig. 7. The displacement of the left end of the wire is constrained, while the right end is pulled such that the specimen attains a total average strain $\bar{\varepsilon}$ of 6.5%, and then the wire is unloaded to $\bar{\varepsilon} = 0$. The total elongation δ of the wire is thus prescribed according to $\delta(t) = L\bar{\varepsilon}(t)$, where $L = 30$ mm is the length of the wire, and the average strain rate $\dot{\bar{\varepsilon}}$ is assumed constant during loading and during unloading, as illustrated in Fig. 7. The applied average strain rate $\dot{\bar{\varepsilon}}$ is varied between 1.1×10^{-4} s^{-1} and 1.1×10^{-1} s^{-1}.

To simulate the heat-sink effect of the grips and to trigger the strain localization in the wire, the temperature of the wire at both ends is fixed and equal to the initial temperature $T_0 = 296$ K.

Material parameters $E = 35$ GPa, $H = -2.2$ MPa, $f_c = 6.8$ MPa, $\bar{\epsilon}_t = 0.049$ and $T_t = 244$ K have been calibrated such that the isothermal stress-strain response of the model approximates the experimental one (Zhang et al., 2010) reasonably well. Parameter $\Delta s^* = 0.24$ MPa/K has been calibrated to correctly represent experimentally observed thermal hardening. Parameters $\rho = 6500$ kg/m^3, $c = 440$ J/(kg K) and $\kappa = 18$ W/(m K) assume the values typical for NiTi (e.g., Armattoe et al., 2016).

The model involves two additional parameters, G and χ, that govern the gradient contribution and the micromorphic regularization. Parameter G defines the thickness of the interface through Eqs. (44) and (40). In principle, the interface thickness, which is expected to be related to the grain size, can be measured, for instance, using the full-field data acquired by DIC (digital image correlation). For example, by interpreting
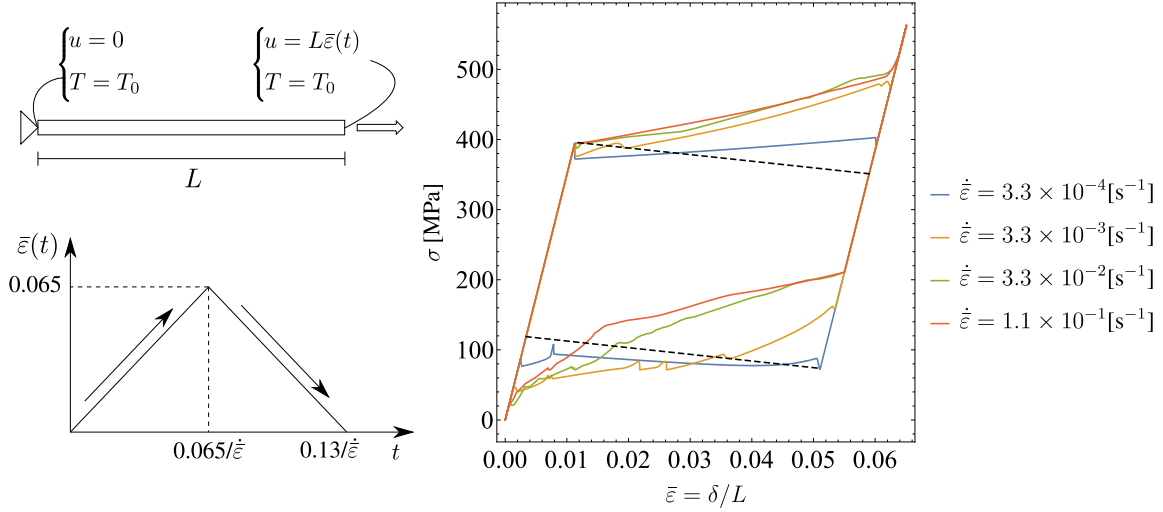
Figure 7: Uniaxial tension of a NiTi wire: problem setup and the predicted stress-average strain response corresponding to four representative average strain rates. The dashed line depicts the isothermal, homogeneous softening response. The average strain $\bar{\varepsilon}$ is defined as the elongation δ divided by the length L.

the strain profiles reported by Kim and Daly (2011, Fig. 10), the thickness of the macroscopic transformation front can be estimated as a fraction of millimeter, say between 0.2 and 0.5 mm. However, in general, experimental identification of the parameters of gradient-enhanced models is not easy and has not been attempted here. Note that, in some situations, it is possible to derive the characteristic length that has a clear physical meaning, for instance, in gradient crystal plasticity, as recently shown by Petryk and Stupkiewicz (2016). To the best of our knowledge, similar relationships are not available for the thickness of the macroscopic transformation front in SMAs.

From a purely computational point of view, the gradient-related parameters are often adopted such that a sufficient regularization is obtained. In particular, the resulting interface thickness cannot be too small compared to the finite-element mesh size, which may be a serious limitation in two- and three-dimensional computations.

In this work, parameter $G = 0.014\,\mathrm{Pa\,m^2}$ has been adopted such that the interface thickness is $\lambda = 0.25$ mm, cf. Eqs. (44) and (40). Parameter $\chi = 116$ MPa has been adopted such that $\bar{\lambda}/\lambda = 0.9$, which holds for $\ell/\lambda = 0.044$ and $\ell = 0.011$ mm, cf. Eq. (57). A relatively fine finite-element mesh of 600 elements has been used in the computations so that the element size $h = 0.05$ mm is sufficiently small with respect to the interface thickness, $\lambda = 5h$.

4.3. Results

The computations have been performed for eleven strain rates, however, only the results obtained for four representative loading rates are discussed in detail. Figure 7 compares the corresponding four curves

17

of stress vs. average strain (called 'stress-strain curves' in the sequel). The elastic loading branch and the point at which the transformation initiates are identical for all curves. During subsequent stages, the effect of loading rate is significant. For the case with the lowest strain rate ($\dot{\bar{\varepsilon}} = 3.3 \times 10^{-4}\ \mathrm{s}^{-1}$), the thermal effect is not much pronounced, and the stress-strain curve is close to the isothermal case, particularly during loading. For higher loading rates, the stress plateau is no longer observed during loading and significant hardening is predicted as a result of the increase in temperature during forward transformation. The effect of loading rate on the unloading branch is more complex. This is due to inhomogeneity of temperature and development of complex transformation patterns that are discussed below.

It is recalled that the rate dependence observed in Fig. 7 is solely due to the thermomechanical coupling and heat conduction. In fact, it is commonly accepted that the thermomechanical coupling is the major effect responsible for the rate dependence in pseudoelastic SMAs at small and moderate strain rates.

The detailed results of individual simulations are depicted in Fig. 8. The first, second and third columns show the stress-strain curves, the transformation patterns and the temperature fields. The dashed curves in the stress-strain diagrams represent the experimental results obtained by Zhang et al. (2010). For the transformation patterns in the middle column, the vertical axis represents the position on the wire, the horizontal axis represents the normalized time, and the color intensity represents the volume fraction of martensite. Similarly, for the temperature field, the color represents the relative temperature $\theta = T - T_0$ as a function of position and time.

The predicted effect of the loading rate on the stress-strain response shows a good agreement with the experiment, particularly considering the simplicity of the constitutive model (with a piecewise-linear isothermal material response) and the approximation introduced by the one-dimensional model and simplified boundary conditions for the temperature. At higher loading rates, the stress predicted during reverse transformation is visibly lower than in the experiment so that the area of the hysteresis loop is overpredicted. This is commented later.

Sudden jumps in the stress-strain curves, which are more visible at lower loading rates, accompany nucleation or annihilation of interfaces and formation of new domains of martensite or austenite. The related effects are in a qualitative agreement with the experiment, as discussed in detail by Zhang et al. (2010).

The middle column in Fig. 8 illustrates the effect of loading rate on the pattern and evolution of austenite and martensite domains. The general feature is that the number of domains increases with increasing loading rate, again in a qualitative agreement with the experiment. It can be seen that the transformation pattern and the number of domains during forward and during reverse transformation are different. This is due to the prior history and non-uniform temperature at the beginning of the unloading stage.

Note that a homogeneous transformation is observed in the central part of the wire for the highest loading rate, see the bluish area in the last row of Fig. 8. At high loading rates, thermal hardening prevails over mechanical softening, and overall hardening hinders strain localization. During the loading process, the
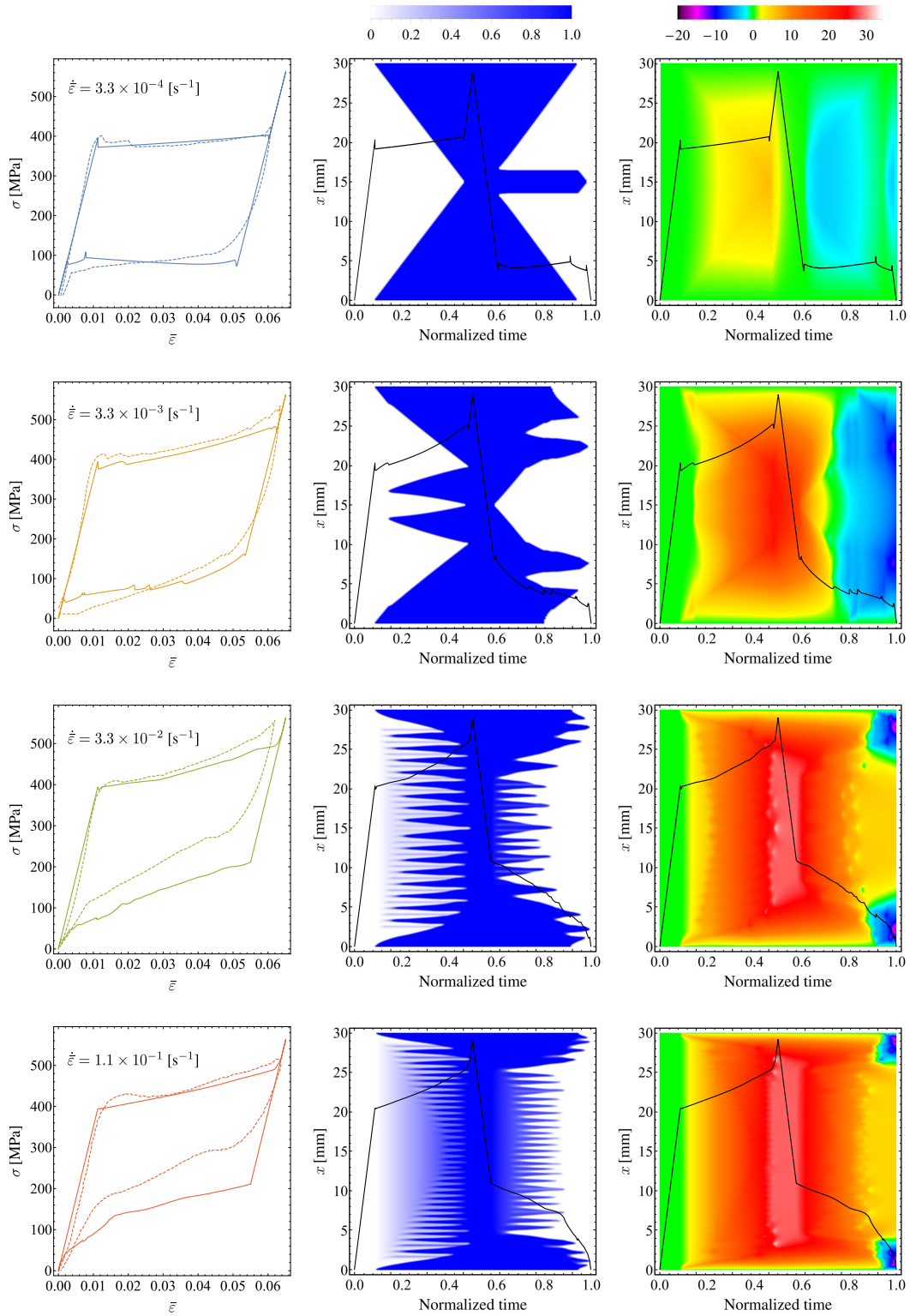
18

Figure 8: Detailed results corresponding to four representative average strain rates: stress-strain response (left), transformation pattern represented by η (middle), relative temperature field (right). The predicted stress-strain response (solid lines) is compared to the experimental results of Zhang et al. (2010) (dashed lines). The solid lines superimposed on the contour plots in the middle and right columns depict the stress as a function of the normalized time.
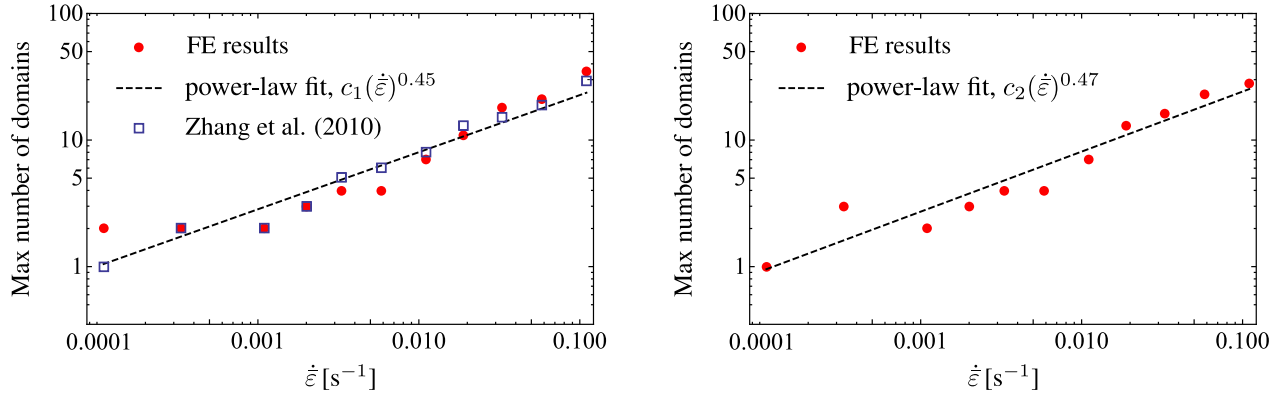
19

Figure 9: The maximum number of martensite domains as a function of the average strain rate $\dot{\bar{\varepsilon}}$ for the forward (left) and reverse (right) transformation. Experimental data of Zhang et al. (2010) is included in the left figure.

zone of homogeneous transformation gradually shrinks at the expense of patterned zones that propagate from both ends of the wire.

It can be seen in Fig. 7 that the solution is symmetric with respect to the wire centre. In all cases, the martensite bands nucleate at the wire ends and are triggered, without any artificial imperfection, by the inhomogeneity of temperature that results from the boundary condition enforced on the temperature at both ends. The symmetry of the solution is then preserved throughout the loading process. This, in particular, implies that, at the lowest strain rates, the forward transformation proceeds by nucleation and propagation of two martensite bands.

The situation is different when the thermomechanical coupling is not included in the model (the corresponding results are not presented in detail). In that case, if no imperfection is introduced, then the martensite bands are not formed, and a homogeneous solution is obtained. An inhomogeneous transformation pattern is obtained only if an imperfection is introduced, and the transformation pattern depends then on the type and position of the imperfection. In particular, if adequately triggered, the transformation may then proceed by nucleation and propagation of a single martensite band.

Figure 9 shows, in a log-log scale, the plot of the maximum number of martensite domains against the average strain rate $\dot{\bar{\varepsilon}}$. It follows that the number of domains is approximately proportional to the square root of the average strain rate with the fitted exponent of 0.45 and 0.47 for the forward and reverse transformation, respectively. These results show a good agreement with the exponent of 0.5 which is characteristic for the experimental data (Zhang et al., 2010). Actually, not only the scaling law, but also the predicted numbers are consistent with those reported by Zhang et al. (2010), see Fig. 9.

The exponent of 0.5 also results from the theoretical analysis of He and Sun (2010) in the case of negligible heat convection. It has also been shown by He and Sun (2010) that, compared to the heat conduction, the effect of heat convection in stagnant air is negligible. Hence, ignoring the effect of heat convection, as
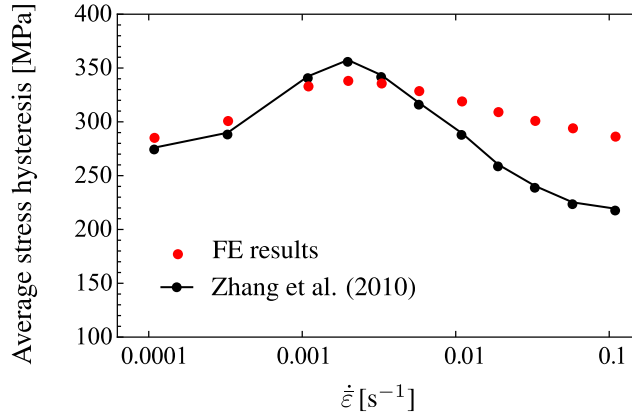
Figure 10: Average stress hysteresis as a function of the average strain rate $\dot{\bar{\varepsilon}}$.

assumed in the present model, does not significantly influence the transformation pattern and the maximum number of domains.

The average stress hysteresis, computed as the area of the hysteresis loop in the stress-strain curve divided by the transformation strain $\bar{\epsilon}_t$, is shown in Fig. 10 as a function of the average strain rate $\dot{\bar{\varepsilon}}$. In agreement with the experimental results that are also included in Fig. 10, the dependence of the average stress hysteresis on the strain rate is not monotonic and exhibits a maximum at the strain rate of about 2×10^{-3} s^{-1}. As already mentioned, the stress hysteresis is overpredicted by the model for high loading rates. A possible reason for this discrepancy is that in the model the transformation is completed upon load reversal while in the experiment it is not necessarily completed. The actual volume fraction of austenite that transforms to martensite during loading may thus be less than unity and may depend on the loading rate (through the average temperature at the reversal point), thus affecting the hysteresis. The related features are not captured by the present simple constitutive model.

Summarizing, despite its simplicity, the present model is capable of reproducing several thermomechanical effects that accompany uniaxial tension of NiTi in a wide range of strain rates. In particular, the proposed micromorphic model proves efficient in modelling nucleation and evolution of complex transformation patterns induced by a softening mechanical response.

5. Conclusions

A micromorphic framework has been developed for modelling of formation and propagation of Lüders-like bands, and strain localization phenomena in general, in pseudoelastic SMAs exhibiting softening. As frequently done in various contexts, a gradient term, here the gradient of the volume fraction of martensite, has been introduced into the constitutive model to avoid ill-posedness of boundary value problems, pathological mesh sensitivity, and related difficulties. A micromorphic regularization has next been performed by

introducing an additional variable as a micromorphic counterpart of the volume fraction of martensite. The incremental energy minimization approach is applied, which results in a compact formulation in the form of a non-smooth constrained minimization problem.

The resulting micromorphic model is suitable for a direct finite-element implementation. The displacement field and the micromorphic counterpart of the volume fraction of martensite constitute the global unknowns that are governed by respective global equations which express mechanical equilibrium and averaging of the local volume fraction of martensite. At the same time, the local volume fraction of martensite is determined individually at each Gauss point, so that efficient techniques, here the augmented Lagrangian method (Stupkiewicz and Petryk, 2013), can be applied locally to treat the complexities related to rate-independent dissipation and physical inequality constraints.

A coupled thermomechanical model has also been developed and used for a finite-element study of the effect of loading rate on the pseudoelastic response and transformation pattern in a NiTi wire. Despite the simplicity of the constitutive model, its predictions show a good agreement with the experiment. In particular, the predicted dependence of the maximum number of martensite domains on the average strain rate satisfies a square-root scaling law that follows from the experiment (Zhang et al., 2010) and from the theoretical considerations (He and Sun, 2010).

The present formulation and finite-element implementation are restricted to one-dimensional problems as the main focus of the present paper is on the gradient-enhancement and its micromorphic regularization. Extension to three dimensions will be reported separately.

References

Ahmadian, H., Ardakani, S.H., Mohammadi, S., 2015. Strain-rate sensitivity of unstable localized phase transformation phenomenon in shape memory alloys using a non-local model. Int. J. Solids Struct. 63.

Aifantis, E.C., 1984. On the microstructural origin of certain inelastic models. J. Eng. Mater. Tech. 106, 326–330.

Alessi, R., Bernardini, D., 2015. Analysis of localization phenomena in Shape Memory Alloys bars by a variational approach. Int. J. Solids Struct. 73, 113–133.

Armattoe, K.M., Bouby, C., Haboussi, M., Ben Zineb, T., 2016. Modeling of latent heat effects on phase transformation in shape memory alloy thin structures. Int. J. Solids Struct. 88, 283–295.

Armattoe, K.M., Haboussi, M., Ben Zineb, T., 2014. A 2D finite element based on a nonlocal constitutive model describing localization and propagation of phase transformation in shape memory alloy thin structures. Int. J. Solids Struct. 51, 1208–1220.

Badnava, H., Kadkhodaei, M., Mashayekhi, M., 2014. A non-local implicit gradient-enhanced model for unstable behaviors of pseudoelastic shape memory alloys in tensile loading. Int. J. Solids Struct. 51, 4015–4025.

Bechle, N.J., Kyriakides, S., 2014. Localization in NiTi tubes under bending. Int. J. Solids Struct. 51, 967–980.

Bhattacharya, K., 2003. Microstructure of martensite: why it forms and how it gives rise to the shape-memory effect. Oxford University Press, Oxford.

de Borst, R., Pamin, J., Geers, M.G.D., 1999. On coupled gradient-dependent plasticity and damage theories with a view to localization analysis. Eur. J. Mech. A-Solids 18, 939–962.

Chang, B.C., Shaw, J., Iadicola, M.A., 2006. Thermodynamics of shape memory alloy wire: Modeling, experiments, and application. Continuum Mech. Thermodyn. 18, 83–118.

Cisse, C., Zaki, W., Zineb, T.B., 2016. A review of constitutive models and modeling techniques for shape memory alloys. Int. J. Plast. 76, 244–284.

Daly, S., Ravichandran, G., Bhattacharya, K., 2007. Stress-induced martensitic phase transformation in thin sheets of Nitinol. Acta. Mater. 55, 3593–3600.

Duval, A., Haboussi, M., Ben Zineb, T., 2011. Modelling of localization and propagation of phase transformation in superelastic SMA by a gradient nonlocal approach. Int. J. Solids Struct. 48, 1879–1893.

Favier, D., Louche, H., Schlosser, P., Orgéas, L., Vacher, P., Debove, L., 2007. Homogeneous and heterogeneous deformation mechanisms in an austenitic polycrystalline Ti–50.8 at.% Ni thin tube under tension. Investigation via temperature and strain fields measurements. Acta. Mater. 55, 5310–5322.

Forest, S., 2016. Nonlinear regularization operators as derived from the micromorphic approach to gradient elasticity, viscoplasticity and damage. Proc. R. Soc. A 472, 20150755.

Geers, M.G.D., 2004. Finite strain logarithmic hyperelasto-plasticity with softening: a strongly non-local implicit gradient framework. Comput. Meth. Appl. Mech. Eng. 193, 3377–3401.

Hallai, J.F., Kyriakides, S., 2013. Underlying material response for Lüders-like instabilities. Int. J. Plast. 47, 1–12.

He, Y.J., Sun, Q.P., 2010. Rate-dependent domain spacing in a stretched NiTi strip. Int. J. Solids Struct. 47, 2775–2783.

Jiang, D., Kyriakides, S., Bechle, N.J., Landis, C.M., 2017a. Bending of pseudoelastic NiTi tubes. Int. J. Solids Struct. 124, 192–214.

Jiang, D., Kyriakides, S., Landis, C.M., 2017b. Propagation of phase transformation fronts in pseudoelastic NiTi tubes under uniaxial tension. Extreme Mech. Lett. 15, 113–121.

Jiang, D., Kyriakides, S., Landis, C.M., Kazinakis, K., 2017c. Modeling of propagation of phase transformation fronts in NiTi under uniaxial tension. Eur. J. Mech. A-Solids 64, 131–142.

Kim, K., Daly, S., 2011. Martensite strain memory in the shape memory alloy nickel-titanium under mechanical cycling. Exp. Mech. 51, 641–652.

Korelc, J., 2009. Automation of primal and sensitivity analysis of transient coupled problems. Comput. Mech. 44, 631–649.

Korelc, J., Wriggers, P., 2016. Automation of finite element methods. Springer International Publishing, Switzerland.

Lagoudas, D.C., Entchev, P.B., Popov, P., Patoor, E., Brinson, L.C., Gao, X., 2006. Shape memory alloys, Part II: Modeling of polycrystals. Mech. Mater. 38, 430–462.

León Baldelli, A.A., Maurini, C., Pham, K., 2015. A gradient approach for the macroscopic modeling of superelasticity in softening shape memory alloys. Int. J. Solids Struct. 52, 45–55.

Mazière, M., Forest, S., 2015. Strain gradient plasticity modeling and finite element simulation of Lüders band formation and propagation. Continuum Mech. Thermodyn. 27, 83–104.

Moreau, J.J., 1974. On unilateral constraints, friction and plasticity, in: Capriz, G., Stampacchia, G. (Eds.), New Variational Techniques in Mathematical Physics. CIME, Edizioni Cremonese, Roma, pp. 175–322.

Mühlhaus, H.B., Boland, J., 1991. A gradient plasticity model for Lüders band propagation. Pure Appl. Geophys. 137, 391–407.

Otsuka, K., Wayman, C.M., 1999. Shape Memory Materials. Cambridge University Press, Cambridge.

Patoor, E., Lagoudas, D.C., Entchev, P.B., Brinson, L.C., Gao, X., 2006. Shape memory alloys, Part I: General properties and modeling of single crystals. Mech. Mater. 38, 391–429.

Peerlings, R.H.J., de Borst, R., Brekelmans, W.A.M., de Vree, J.H.P., 1996. Gradient enhanced damage for quasi-brittle materials. Int. J. Numer. Meth. Eng. 39, 3391–3403.

Petryk, H., 2003. Incremental energy minimization in dissipative solids. Compt. Rendus. Mec. 331, 469–474.

Petryk, H., Stupkiewicz, S., 2016. A minimal gradient-enhancement of the classical continuum theory of crystal plasticity. Part I: The hardening law. Arch. Mech. 68, 459–485.

Pieczyska, E.A., Gadaj, S.P., Nowacki, W.K., Tobushi, H., 2006. Phase-transformation fronts evolution for stress-and strain-controlled tension tests in TiNi shape memory alloy. Exp. Mech. 46, 531–542.

Raniecki, B., Lexcellent, C., Tanaka, K., 1992. Thermodynamic models of pseudoelastic behaviour of shape memory alloys. Arch. Mech. 44, 261–284.

Rockafellar, R.T., 1970. Convex Analysis. Princeton University Press, Princeton, New Jersey.

Sedmák, P., Pilch, J., Heller, L., Kopeček, J., Wright, J., Sedlák, P., Frost, M., Šittner, P., 2016. Grain-resolved analysis of localized deformation in nickel-titanium wire under tensile load. Science 353, 559–562.

Shaw, J.A., Kyriakides, S., 1997. On the nucleation and propagation of phase transformation fronts in a NiTi alloy. Acta. Mater. 45, 683–700.

Sittner, P., Liu, Y., Novák, V., 2005. On the origin of Lüders-like deformation of NiTi shape memory alloys. Int. J. Solids Struct. 53, 1719–1746.

Steinbach, I., 2009. Phase-field models in materials science. Model. Simulat. Mater. Sci. Eng. 17, 073001.

Stupkiewicz, S., Petryk, H., 2013. A robust model of pseudoelasticity in shape memory alloys. Int. J. Numer. Meth. Eng. 93, 747–769.

Sun, Q.P., Li, Z.Q., 2002. Phase transformation in superelastic NiTi polycrystalline micro-tubes under tension and torsion—from localization to homogeneous deformation. Int. J. Solids Struct. 39, 3797–3809.

Tůma, K., Stupkiewicz, S., Petryk, H., 2017. Rate-independent dissipation in phase-field modelling of displacive transformations (submitted for publication).

Zhang, X., Feng, P., He, Y., Yu, T., Sun, Q.P., 2010. Experimental study on rate dependence of macroscopic domain and stress hysteresis in NiTi shape memory alloy strips. Int. J. Mech. Sci. 52, 1660–1670.